Toward an Objective Analysis of Rainfall Rate Combining Observations and Short-Term Forecast Model Estimates

LOUIS GARAND

Atmospheric Environment Service, Dorval, Quebec, Canada

CHRISTOPHER GRASSOTTI

Atmospheric and Environmental Research, Inc., Cambridge, Massachusetts

(Manuscript received 24 October 1994, in final form 7 March 1995)

ABSTRACT

This study explores the feasibility of performing an objective analysis of instantaneous rain rate combining satellite estimates (and eventually other types of observations) with those from a numerical prediction model using the method of statistical interpolation. Results demonstrate that the quality of the short-term precipitation forecasts serving as background field has reached a level that makes such an objective analysis possible.

The two main requirements to obtain an accurate analysis from available information are a realistic estimate of background field and observation errors and knowledge of the horizontal correlation of these errors with distance. The importance of specifying the errors for joint model-observation situations is emphasized; it is especially important in situations where model and observations are in conflict. These aspects of the problem are studied using collocated 6-h forecasts with satellite estimates derived from visible and infrared imagery, and ground-truth rainfall data available over Japanese territory from the Global Precipitation Climatology Project. Over 90 000 truth–model–satellite collocations are available at the common scale of 130 km × 130 km. An alternative means of establishing the model error correlation with distance and azimuth direction from 6- and 18-h forecast differences valid at the same time yield results that are similar to those derived from collocations with truth rainfall over large domains, but not locally; this result suggests a means of relaxing the assumption of homogeneity and isotropy of model errors. The sensitivity of the rain rate analysis to different specifications of the satellite to model error ratios is shown with an example.

1. Introduction

In meteorology, the goal of objective analysis is to combine observations with a background field, usually a 6-h forecast, to produce an analysis on a regular grid. The objective analysis method most widely used in numerical weather prediction (NWP) centers is that of "optimum" or "statistical interpolation" (SI; see, e.g., Rutherford 1972; Lorenc 1981). More recently, analysis procedures based on variational methods have been adopted in a number of centers, aiming at an eventual 4D assimilation; their 3D version gives results that are largely equivalent to the SI method. The interested reader can appreciate the growing importance of data assimilation in the recent literature (Daley 1991; Courtier et al. 1993). The central problem in SI is the specification of both background and observation errors and their covariance since these determine their relative weight. A good part of today's research aims at better estimating or predicting these errors locally.

In this paper, we address the subject of objective analysis of near-instantaneous rainfall rate using a univariate SI methodology. This approach is usually chosen in NWP centers to analyze humidity, while the mass and wind fields are analyzed in a multivariate manner (see, e.g., Shaw et al. 1987; Mitchell et al. 1990). Up to now, few researchers have attempted an objective analysis of rainfall rate. Tanguay and Robert (1990) used SI principles to analyze 24-h accumulations from surface observations with a zero background field. Recently, Bhargava and Danard (1994) went further by analyzing 24-h accumulations combined with a background field produced by a mesoscale model at 25-km resolution. Grassotti and Garand (1994; hereafter GG94) showed that model instantaneous estimates can be combined with satellite estimates to get an improved estimate, provided the model is used in situations where it performs the best. This paper continues the work of GG94 but within the framework of objective analysis. We are not aware of other publications combining models and observations of instantaneous rainfall. The main reason for this is certainly the difficulty in obtaining good ground truth of rainfall at a scale commensurate with that of the forecast

Corresponding author address: Dr. Louis Garand, Atmospheric Environment Service, 2121 Trans-Canada Highway, Dorval, Quebec, Canada H9P1J3.

model. In addition, the SI approach is suitable only if the model achieves a level of accuracy comparable to that of the observations and vice versa. The GG94 study showed that this is indeed generally the case.

The error specification of rainfall is inherently difficult because it is a discontinuous field; errors are certainly higher statistically where rain is forecasted than where it is not. In addition, significant rainfall variations are observed at scales smaller than the analysis grid; that problem will be minimized by using, whenever possible, observations representative of the analysis horizontal scale. The model will also suffer some phase errors resulting in conflicting rain/no-rain situations from model and observations. It therefore seems logical to establish some error categories as well as joint model-observation categories rather than to simply rely on one overall estimate, independent of the synoptic situation, for the model and observation errors.

We start in section 2 by expressing the basic SI formulation. The operational Canadian Meteorological Center (CMC) spectral forecast model is used in collocation with observed ground truth from the first algorithm intercomparison project (AIP-1) of the Global Precipitation Climatology Project (GPCP), which was held over Japan. In addition, visible and infrared satellite estimates of rainfall based on the GG94 scheme are also available in collocation with the truth dataset. The scale of this combined model–satellite–truth rainfall dataset is 1.25° latitude × 1.25° longitude (130 km). The model and satellite errors are established as a function of cloud type. In addition, the ratio of satellite-to-model errors is established for broad joint model–satellite categories of rainfall estimates. The correlation of the errors with distance for both model and satellite estimates is also derived from the collocated datasets. An alternative means of computing the horizontal correlation of model errors using differences of 6- and 18-h forecasts valid at the same time is also explored. This section is presented with a view toward the future, hinting at the possibility of predicting model errors locally and relaxing the current assumption of isotropy and homogeneity of the error. In section 3, examples of rain analysis are shown, highlighting the sensitivity to differing model and satellite errors. The article concludes with a discussion on means to achieve an operational implementation in the near future.

2. Data analysis

a. Statistical interpolation

In SI, the analysis A is a correction to the background (or guess) field G, a short-term forecast, via the equation:

$$A = G + \sum_{i=1,N} W_i f_i, \tag{1}$$

with $f_i = O_i - G_i$, where i is the site of observations O_i, N is their number, G_i is an interpolation of the background to the observation site, and W_i is the weight to be given to each proposed analysis increment f_i. Assuming observation and background errors are uncorrelated, the system of linear equations defining the weights W_i can be written in dimensional form in terms of background (**B**) and observation (**O**) error covariance matrices:

$$\sum_{j=1,N} (B_{ij} + O_{ij})W_j = B_{ai}; \quad i = 1, N. \tag{2a}$$

In nondimensional form expressed in terms of error correlations, (2a) becomes

$$\sum_{j=1,N} \left[\mu_{ij} \frac{\sigma_{bj}}{\sigma_{bi}} + \nu_{ij}\sigma_{0i} \frac{\sigma_{0j}}{\sigma_{bi}^2} \right] W_j = \mu_{ai} \frac{\sigma_{ba}}{\sigma_{bi}}; \quad i = 1, N, \tag{2b}$$

where $\mu_{ij} = B_{ij}(\sigma_{bi}\sigma_{bj})^{-1}$ is the horizontal correlation of background errors between sites i and j, and ν_{ij} is the corresponding horizontal correlation of observation errors; σ_{0i} and σ_{bi} are, respectively, the observation and background rms errors at site i, and a designates the analysis gridpoint location. The customary assumption of a uniform background error around the analysis grid point further reduces the complexity of (2b) significantly ($\sigma_{ba} = \sigma_{bi} = \sigma_{bj}$) and evidences the importance of the variance ratio $(\sigma_0/\sigma_b)^2$ in the determination of the weights.

While the quality of the analysis will be directly dependent on the quality of the background and observation estimates, the analysis will be optimum in a least squares sense if the weights of (2) are used. It should be noted that (2) implies that there is no statistical bias in the model or observation estimates, a situation difficult to achieve in general and for precipitation especially. Care must be taken to recognize sources of potential biases in precipitation data. Satellite estimates, for example, need to be validated in different regions and seasons (Arkin and Xie 1994).

In (2b), the horizontal correlations of errors are assumed to be a function of distance alone and isotropic. For humidity (Mitchell et al. 1990) and for precipitation (as found in this study), the model and observation horizontal error correlations can be modeled by the equation

$$C_{ij} = \left(1 + \frac{D_{ij}}{L}\right) \exp\left(-\frac{D_{ij}}{L}\right), \tag{3}$$

where D_{ij} is the distance and L is a length scale to be determined by a fit to the data. Thousands of collocations (model and truth) binned by distance are usually necessary to obtain a good fit. Previous studies using surface observations of rainfall did not consider the horizontal correlation of observation errors. This is probably reasonable in that context, but for satellite estimates originating from a single instrument, one needs to account for this correlation (Garand 1994; Sullivan et al. 1993).

Equation (2) is general and can be used with any ensemble of observations. However, for the purpose of this study, we will consider only satellite estimates derived from visible and infrared imagery. To minimize the horizontal-scale representativeness error, an effort was made to use both observations and forecast model estimates at approximately the same horizontal scale as the analysis grid.

b. Datasets

The collocated truth–model–satellite datasets used in this study are as described in GG94. The same ground-truth data were used by Adler et al. (1993), Negri and Adler (1993), and other participants of AIP-1 (Arkin and Xie 1994). The collocated datasets are all at the scale of 1.25° latitude × 1.25° longitude. The hourly verification rainfall data were available for June 1989 (715 h) and for the period 15 July–15 August 1989 (747 h). We used the same 63 1.25° areas as in GG94 (see their Fig. 1), which implies over 45 000 observations in each month. The truth rainfall data are a composite of radar and rain gauges, with ongoing calibration of the former by the latter, as described in Negri and Adler (1993). Over 13 000 rain gauges are used together with 25 radars. This represents one of the best truth rainfall dataset that exists at hourly scale over such an extended domain. In this paper we consider these 1-h accumulations as instantaneous estimates.

TABLE 1a. Class statistics in June for the VIS–IR scheme. Listed are the mean observed "truth" probability of precipitation POP_t (%) and rain rate RR_t, the mean background (RR_b) and satellite rain rate (RR_s), and the corresponding error standard deviation from truth (mm h^{-1}): σ_b and σ_s. Satellite-to-background rms error ratio are also shown.

Class	N	POP_t	RR_t	RR_b	RR_s	σ_b	σ_s	σ_s/σ_b
1	866	9.1	0.03	0.20	0.05	0.36	0.16	0.44
2	222	11.7	0.02	0.23	0.02	0.29	0.06	0.21
3	530	17.7	0.06	0.24	0.10	0.43	0.21	0.49
4	399	21.8	0.05	0.17	0.05	0.26	0.12	0.46
5	314	6.4	0.01	0.13	0.01	0.22	0.06	0.27
6	621	1.8	0.00	0.10	0.01	0.21	0.04	0.19
7	392	11.5	0.04	0.18	0.05	0.35	0.16	0.46
8	1203	66.3	0.64	0.55	0.65	1.00	1.01	1.01
9	503	23.3	0.09	0.25	0.12	0.37	0.31	0.84
10	422	3.3	0.01	0.15	0.01	0.27	0.06	0.22
11	708	1.7	0.01	0.11	0.01	0.27	0.09	0.33
12	313	17.6	0.08	0.21	0.12	0.45	0.30	0.67
13	621	47.8	0.25	0.31	0.28	0.50	0.44	0.88
14	367	4.9	0.01	0.11	0.01	0.19	0.04	0.21
15	1023	90.5	1.89	0.88	2.07	1.71	1.83	1.07
16	705	1.3	0.00	0.11	0.00	0.26	0.02	0.08
17	364	5.5	0.03	0.16	0.06	0.38	0.19	0.50
18	253	1.2	0.00	0.11	0.00	0.21	0.02	0.09
19	1080	37.9	0.26	0.40	0.31	0.74	0.64	0.86
20	461	69.6	0.54	0.44	0.59	0.66	0.75	1.13
21	5628	0.4	0.00	0.04	0.00	0.12	0.03	0.25
22	15	100.0	3.47	1.09	4.00	2.00	1.26	0.63

TABLE 1b. Same as Table 1a but for the IR (night) scheme.

Class	N	POP_t	RR_t	RR_b	RR_s	σ_b	σ_s	σ_s/σ_b
1	2069	56.4	1.13	0.62	1.43	1.58	1.79	1.13
2	637	7.4	0.02	0.07	0.03	0.21	0.12	0.57
3	861	31.0	0.12	0.13	0.11	0.26	0.29	1.11
4	199	3.0	0.01	0.02	0.02	0.07	0.06	0.85
5	627	5.3	0.02	0.05	0.03	0.17	0.15	0.88
6	327	4.9	0.01	0.04	0.01	0.10	0.05	0.50
7	341	12.6	0.03	0.09	0.05	0.14	0.10	0.71
8	512	10.2	0.03	0.05	0.04	0.18	0.12	0.67
9	402	11.7	0.03	0.06	0.02	0.15	0.10	0.67
10	562	9.3	0.05	0.09	0.06	0.32	0.28	0.87
11	597	6.2	0.01	0.04	0.03	0.13	0.05	0.38
12	584	4.6	0.01	0.04	0.03	0.14	0.07	0.50
13	225	5.8	0.02	0.06	0.01	0.19	0.08	0.42
14	281	2.1	0.00	0.05	0.00	0.10	0.02	0.20
15	898	10.7	0.06	0.08	0.09	0.30	0.27	0.90
16	5402	37.3	0.41	0.37	0.48	0.78	0.96	1.23
17	1578	26.7	0.15	0.15	0.22	0.41	0.43	1.05
18	3743	27.9	0.17	0.21	0.25	0.46	0.53	1.15
19	304	5.9	0.04	0.06	0.04	0.21	0.23	1.09
20	679	13.1	0.04	0.06	0.04	0.20	0.17	0.85
21	7125	1.0	0.00	0.02	0.00	0.07	0.03	0.42
22	82	91.5	4.28	1.41	4.00	2.60	2.42	0.93

The model 6-h forecast rainfall rates were obtained using the CMC spectral forecast model with 21 vertical levels and 106 wavenumbers. Forecasts were then interpolated to the 1.25° grid. Model estimates inbetween the 6-h forecasts were interpolated in time to get values at every hour. (This is not ideal, but the submission of forecasts every hour in order to get true 6-h forecasts at all hours is not practical.) The satellite estimates used in this study are based on the method presented in GG94. The last 15 days of June were used to develop the technique, so that this month represents half-dependent data, while the July–August data are fully independent data. The method is based on cloud classification and uses visible (VIS) and infrared (IR) imagery leading to a VIS–IR scheme and to an IR alone scheme for nighttime retrievals. The classification is made from only three parameters: cloud fraction (CF), cloud-top pressure (CTP), and cloud albedo (AL), the latter being used only for the VIS scheme. Both schemes (IR and VIS–IR) have 20 classes, and a mean rain rate is associated to each class. The two schemes are defined in Tables 1 and 2 of GG94 in terms of AL, CF, CTP, and rain rate means. For each scheme, there are two additional classes: class 21 defines all fields with a cloud fraction less than 30%—a zero rain rate is assigned in that class; and class 22 defines all fields with a CTP less than 170 mb—these very cold clouds (cumulonimbus) are assigned a rain rate of 4 mm h^{-1}. Both the truth dataset and the model dataset only rarely will have rainfall rates superior to 4 mm h^{-1}. As one would expect, the GG94 scheme reflects the fact that rain rates tend to be higher with colder and more reflective clouds.

TABLE 2. Rain-rate error standard deviation (σ) and bias (BI) by joint model–satellite categories for June (J) and July/August (JA) infrared (IR) and VIS–IR (VIR) schemes. The four categories of background (b) and satellite (s) estimates (mm h^{-1}) are 1) RR_s and $RR_b > 0.1$; 2) $RR_s > 0.3$ and $RR_b < 0.1$; 3) $RR_s < 0.05$ and $RR_b > 0.3$; 4) all other cases. Error ratio σ_s/σ_b, mean observed "truth" rainfall rate RR_t, and number of samples N are also listed.

Category	Data	N	RR_t	BI_b	BI_s	σ_b	σ_s	σ_s/σ_b
1	J-VIR	3687	0.85	−0.16	−0.01	1.24	1.16	0.93
2	J-VIR	888	0.35	−0.32	0.32	0.82	0.77	0.94
3	J-VIR	886	0.03	0.59	−0.12	0.39	0.13	0.33
4	J-VIR	11 549	0.01	0.04	0.01	0.18	0.11	0.61
1	J-IR	6649	0.82	−0.16	−0.17	1.26	1.30	1.03
2	J-IR	3105	0.09	−0.06	0.54	0.40	0.59	1.47
3	J-IR	1107	0.11	0.50	−0.09	0.48	0.34	0.71
4	J-IR	18 028	0.02	0.00	0.04	0.15	0.15	1.00
1	JA-VIR	1499	1.15	−0.20	−0.52	1.87	1.44	0.77
2	JA-VIR	409	1.13	−1.11	−0.42	1.75	1.59	0.91
3	JA-VIR	1980	0.08	0.67	−0.08	0.52	0.24	0.46
4	JA-VIR	13 878	0.06	0.03	−0.04	0.35	0.23	0.66
1	JA-IR	2683	0.78	−0.12	−0.15	1.71	1.36	0.79
2	JA-IR	1537	0.90	−0.89	−0.01	1.67	1.49	0.89
3	JA-IR	1417	0.18	0.65	−0.17	0.72	0.47	0.65
4	JA-IR	23 658	0.07	−0.03	−0.03	0.31	0.29	0.94

c. *Model and satellite errors*

As mentioned earlier, it is desirable to detail the background and observation rainfall errors in order to consider to some degree the weather situation. This is in contrast to common NWP practice where the errors related to meteorological variables may depend on latitude and season but not on the actual synoptic situation. Here we use cloud classification as a means to categorize the synoptic situation: model and satellite errors are estimated in each class. Table 1 presents these errors for VIS–IR and IR classifiers, along with the observed probability of rainfall and the mean observed and model rain rate associated with each class. Here, RR_s is the class rain rate inferred by the GG94 algorithm. The number of samples is of the order of several hundreds for most classes. While it is immediately apparent that the absolute error increases with the average value of the inferred rainfall (an expected result), this, in itself, is not the primary reason for defining error categories. Indeed, the important term in (2) is the ratio σ_0/σ_b rather than σ_0 and σ_b individually. The last column in Table 1 lists this ratio (where $\sigma_0 = \sigma_s$). It is noted, for both the IR and VIS–IR schemes, that the satellite retrievals are clearly superior to the model estimates in classes of low or no rainfall. However in classes of moderate rain rates, such as 8 and 15 of the VIS–IR scheme and 1, 3, and 16–19 of the IR scheme, the model estimates are of equal or superior quality to the satellite estimates. In July/August (errors not shown by class but broader categories will be discussed further), the model was systematically poorer than the satellite retrievals; nevertheless, it performed best in classes just mentioned, with error ratios in the range 0.7 to 0.9. Class 22, deep cumulonimbus, is important because of the high rainfall rate associated with it. For the 82 samples of the IR scheme, the error standard deviations σ_b and σ_s are similar, but the model suffers a large negative bias. This occurs because the model cannot localize storms as precisely as the satellite. The probability of precipitation (POP) in Table 1 is a score of detection of rain versus no rain, with highest uncertainty at POP = 50%. In class 22, the POP exceeds 90%. To account for the model difficulty in locating deep cumulonimbus, the satellite to model error ratio should be of the order of 0.5 in cases where the model infers no rain, while class 22 is observed.

The classification process used here is just one way to categorize the error. Perhaps the categorization is too detailed since classes associated with significant rainfall have similar error ratios. The key concept is that of *joint model–satellite* categories. In Table 1, the model and satellite errors are linked by the classification process. Another way, less detailed but more generally applicable, to link model and satellite error estimates in order to improve the determination of σ_s/σ_b is to define broad joint categories. Four categories come to mind:

1) model and satellite agree on significant rainfall;
2) model infers little or no rainfall, but satellite infers significant rainfall;
3) model infers significant rainfall, but satellite infers little or no rainfall;
4) all other cases (mostly little or no rainfall from model and observations).

Table 2 presents the statistics for these broad categories, for both schemes and for the two monthly periods. The thresholds defining the categories are spec-

ified in the table caption. The ground truth average rain rate RR_t was higher in July/August, characterized by less frequent but more intense rainfall, than in June when stratiform rain prevailed. Model and satellite errors were both higher in July/August than in June. However, the error ratio σ_s/σ_b of the VIS–IR scheme was similar for both time periods. The error ratios were not too different either for the IR scheme of both periods, except in category 2. There were many false alarms in June, resulting in the 0.54 mm h^{-1} bias in category 2, but little bias occurred in July/August. This bias was due mostly to the significant IR rain classes 1 and 16, in which the observed probabilities of rainfall were, respectively, 56% and 37% in June, but much higher in July/August: 78% and 54%, respectively. Due to this uncertainty in the relative model and satellite errors, an error ratio of unity could be imposed in category 2 of the IR scheme, implying a resulting analysis that will be a compromise between two conflicting estimates. It is worth noting that the occurrence of conflicting situations, that is, categories 2 and 3, accounts for a relatively modest 10%–13% of the cases. This is quite encouraging for the eventual implementation of an operational rainfall analysis.

In each period, the error ratio is significantly less for the VIS–IR scheme than it is for the IR scheme, a result that is indicative of the true utility of the visible channel for rain inference (see Cheng et al. 1993, who support this conclusion). Another tangible result is the clear superiority of the satellite in the conflict category 3. The VIS–IR rms error ratio is as low as about 0.40 [variance ratio of 0.16, equivalent from Eq. (2) to a weight of 0.86 for a single observational increment at the analysis grid point]. This simply reflects the fact that the satellite is very good in detecting regions with no precipitation: its negative bias is small, whereas the positive bias of the model is of the order of 0.6 mm h^{-1} in category 3. Imposing these low error ratios in these situations will minimize the negative influence of model phase errors. The significant differences in error ratios among the categories in Tables 1 and 2 demonstrate the utility of the categorization.

d. Model and satellite horizontal correlation of errors

1) CLASSICAL APPROACH

The horizontal covariance of model or satellite rain rate errors is computed from

$$\mathrm{cov}(i,j) = \overline{E_i E_j} - \overline{E_i}\,\overline{E_j}, \qquad (4)$$

where E_i is the error at site i, that is, the deviation of the model or satellite estimate from the radar–rain gauge observation. The covariance was computed from the 63 contiguous 1.25° × 1.25° areas in distance bins between sites i and j. The results are presented in Table 3 for the two time periods and for all hours. The covariance is negligible beyond 700 km and is not listed.

TABLE 3. Model and satellite (Sat) rain rate error autocovariance [(mm h^{-1})^2] as a function of distance (km) for June and July/August: N—number of samples. Corresponding length scales (km) fitted from Eq. (3) are also listed.

	June			July/August		
Distance	N	Model	Sat	N	Model	Sat
0	45 045	0.422	0.436	47 061	0.581	0.349
126.0	72 930	0.177	0.207	76 194	0.283	0.119
179.2	64 350	0.096	0.136	67 230	0.172	0.058
264.9	126 555	0.027	0.068	132 219	0.053	0.012
345.2	140 855	−0.006	0.031	147 159	0.025	0.005
450.1	177 320	−0.011	0.001	185 256	−0.011	−0.003
557.8	137 995	−0.003	0.003	144 171	−0.012	0.003
696.6	231 660	−0.002	0.002	242 028	−0.002	0.005
L_b, L_0		66.2	80.0		74.3	58.8

The satellite estimates were derived from the IR scheme at night and from the VIS–IR scheme in daytime. The bin at distance 126 km represents all pairs one grid point away from one another. From Table 3, at zero distance it is noted that the model and satellite had very similar error variances in June (corresponding to a rms error of 0.65 mm h^{-1}), whereas satellite estimates were significantly superior to model estimates in July/August. The data from Table 3 were fitted using (3). The resulting fits are shown in Fig. 1. It is seen that the function chosen fits the data satisfactorily. The same function was used by Sullivan et al. (1993) to fit temperature retrieval errors from polar-orbiting satellites. This function is also used at CMC to fit humidity errors (Garand 1994). The Gaussian hill function used by Tanguay and Robert (1990) was also tried, resulting in reasonable fits. However, that function appeared to decrease somewhat too slowly at short distances and too sharply at larger distances (150 km and beyond).

The radar–rain gauge "truth" dataset is obviously not free from errors. Assuming that radar–rain gauge errors at various sites are not correlated horizontally means that the error component associated with the verification dataset is zero in (4), except at zero distance, where the covariance error represents the sum of the model or satellite errors and that of the radar–rain gauge. One way to separate the two errors is to ignore the zero distance data and to fit the function with the other bins only (Mitchell et al. 1990). The intercept at zero distance then represents the "true" model error, and the difference between the total error and the intercept represents the error of the verification dataset. This was tried, but for three of the four curves in Fig. 1, the intercept ended up slightly above the total error, which cannot be, but is indicative of a low error for the verification dataset. One curve yielded a radar–rain gauge error variance of 0.05 (mm h^{-1})^2. Based on this, it was assumed that the radar–rain gauge error variance was 0.04 (mm h^{-1})^2 or a rms of 0.2 mm h^{-1}. This number can be compared with the discretization

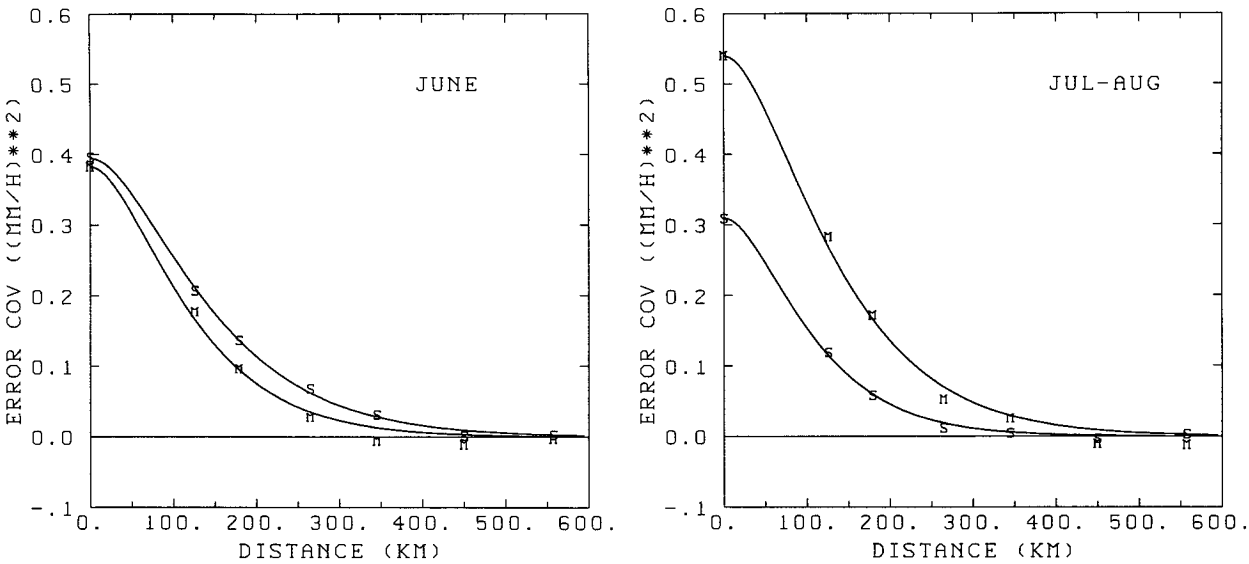

FIG. 1. (a) Rain-rate error covariance as a function of distance for the June dataset: S and M designate the satellite and model background bin values (Table 3). (b) Same as (a) but for the July–August dataset.

of the radar–rain gauge data of 0.1 mm h^{-1} and with the approximate 0.7 mm h^{-1} model or satellite errors. The M and S at zero distance in Fig. 1 represent the total error (model or satellite plus radar–rain gauge) as listed in Table 3 lowered by 0.04. The excellent quality of the verification dataset is the result of the ongoing calibration process with a large number of rain gauges and of the spatial and temporal averaging of observed high-resolution rain rates to hourly values on the 1.25° grid, which minimizes an otherwise important representativeness error. Thus, it appears justifiable to compute error standard deviations, as was done in Tables 1 and 2, assuming a negligible error for the verification dataset. The quantity of importance in SI, the error variance ratio, would be insensitive to a verification dataset error of that magnitude.

The effect of the length scales is also important. As seen in Table 3, the resulting length scales (L_0 and L_b) are consistent in the two datasets. When compared with June, L_0 slightly increases in July/August, whereas the reverse is true for L_b. The average of the two months suggests a value of about 70 km for both L_0 and L_b. Separating the data into low and high rain rates to get varying length scales did not appear to be warranted in the sense that the resulting length scales varied only marginally (about 15%) for both satellite and model. Using $L_0 = L_b$ in all conditions greatly simplifies the interpretation of the analysis resulting from (2). It means that the weights are controlled almost entirely by the satellite-to-model error ratio, and the role of the length scale is to define a smoothing influence up to about $2.5L$. It is known (see, e.g., Daley 1991; Garand 1994) that ignoring the horizontal error correlation for observations increases the relative weight of the observations with respect to the background, and this effect increases with the density of observations. In more general terms, with σ_0/σ_b equal to unity, the weight of the observation increases if $L_0 < L_b$ and it decreases otherwise. Thus, the ratio L_0/L_b may amplify or counteract the effect suggested by a ratio σ_0/σ_b that differs from unity.

2) ALTERNATIVE APPROACH TO INFER MODEL ERRORS

The classical approach just described requires a truth dataset. For precipitation, gathering truth data at similar resolution to that of forecast models is not an easy task. Also, the errors need to be evaluated over different regions of the globe, by season, etc. Furthermore, truth data being typically sparse, it is difficult to obtain 2D error correlations in order to validate the hypothesis of isotropy. To infer model errors, one idea that is currently being investigated at forecasting centers (Parrish and Derber 1992) is that of using differences of forecasts valid at the same time but issued 12 or 24 h apart, for example, differences between 24- and 48-h forecasts valid at the same time. The differences between the two forecasts results solely from the different state of the model at the initial time of the shortest of the two forecasts; this difference can be seen as a perturbation of the initial state, and it is hypothesized that the resulting forecast differences provide a good picture of the model error. Because no actual truth is used, it is clear that such a method cannot yield the right absolute value of the error variance. However, the hypotheses of interest are that

1) scaling the resulting maps of model error to a realistic values is possible;

2) the horizontal (as well as vertical for 3D fields) correlation of forecast errors can be inferred to very good accuracy with this method.

Our own investigation at the CMC of the second hypothesis looks promising in that horizontal and vertical correlations are indeed very similar to those obtained by the classical method. Similar findings were obtained at the European Centre for Medium-Range Weather Forecasts (ECMWF; Rabier and McNally 1993).

Here we examine the horizontal correlation of errors from the difference between a 6- and an 18-h forecast both valid at 0600 UTC 27 June 1994. Normally, an ensemble of such forecast pairs would be required, but since we only examine here the horizontal correlation of errors (not the horizontal patterns of σ_b), one example provides a sample size sufficient for illustration purposes. The CMC spectral model currently uses 360 $\times$ 180 points on a Gaussian grid at 1° resolution, which permits one to obtain a large number of pairs at various distances from a single forecast. The error covariance can be obtained by Eq. (4). However, a fast approach exists for this calculation of the autocorrelation over a gridded domain. Indeed, a result often used in image processing is that the (discrete) autocorrelation of a field $f(x, y)$ is the inverse Fourier transform of the power spectrum of the field (see Rosenfeld and Kak 1982), so that the sequence of calculations is the following:

1) compute the discrete Fourier transform $f(u, v)$ of the field $f(x, y)$ represented by the difference between the 6- and 18-h forecasts with the overall bias removed;

2) compute the inverse Fourier transform of the power spectrum $|f(u, v)|^2$, and normalize (its real part) with the (0, 0) component to get the autocorrelation.

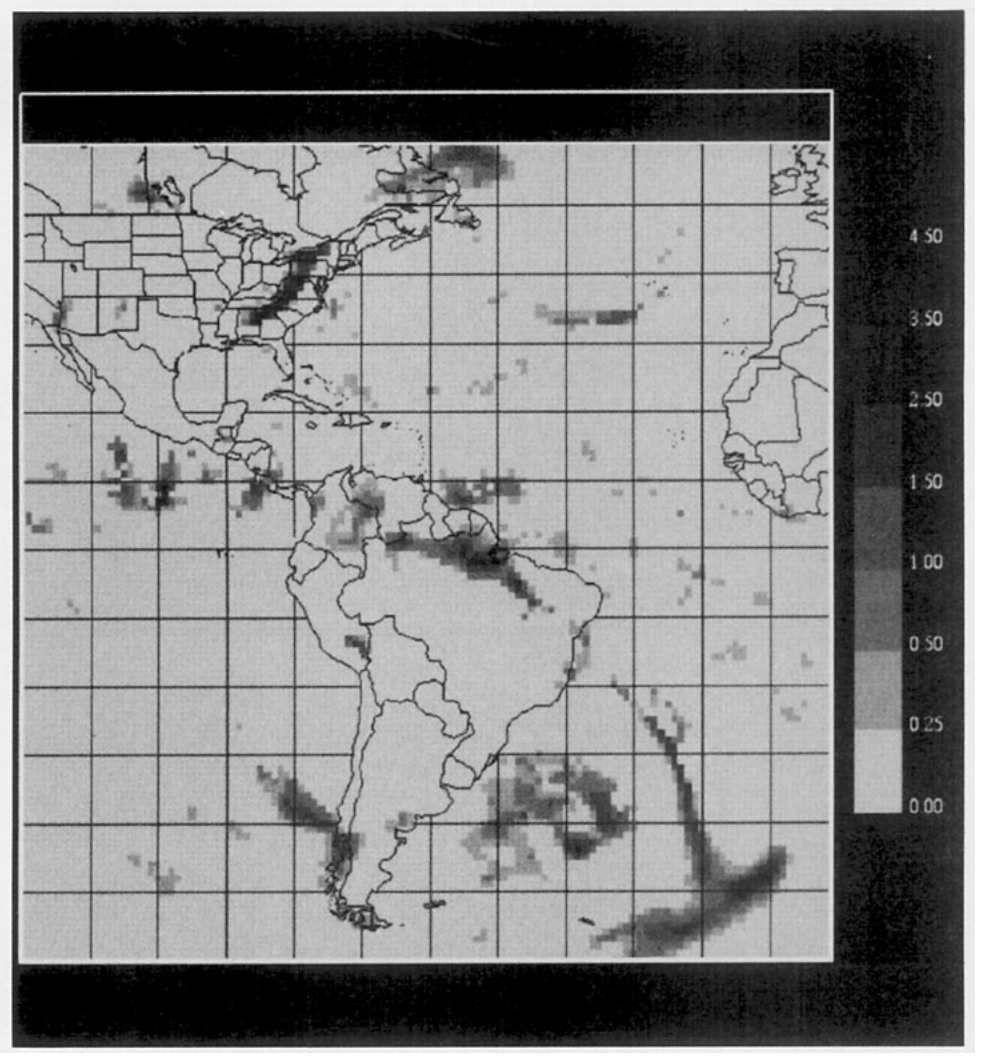

FIG. 2. The 6-h forecast rain rate (mm h^{-1}) valid at 0000 UTC 27 June 1994.

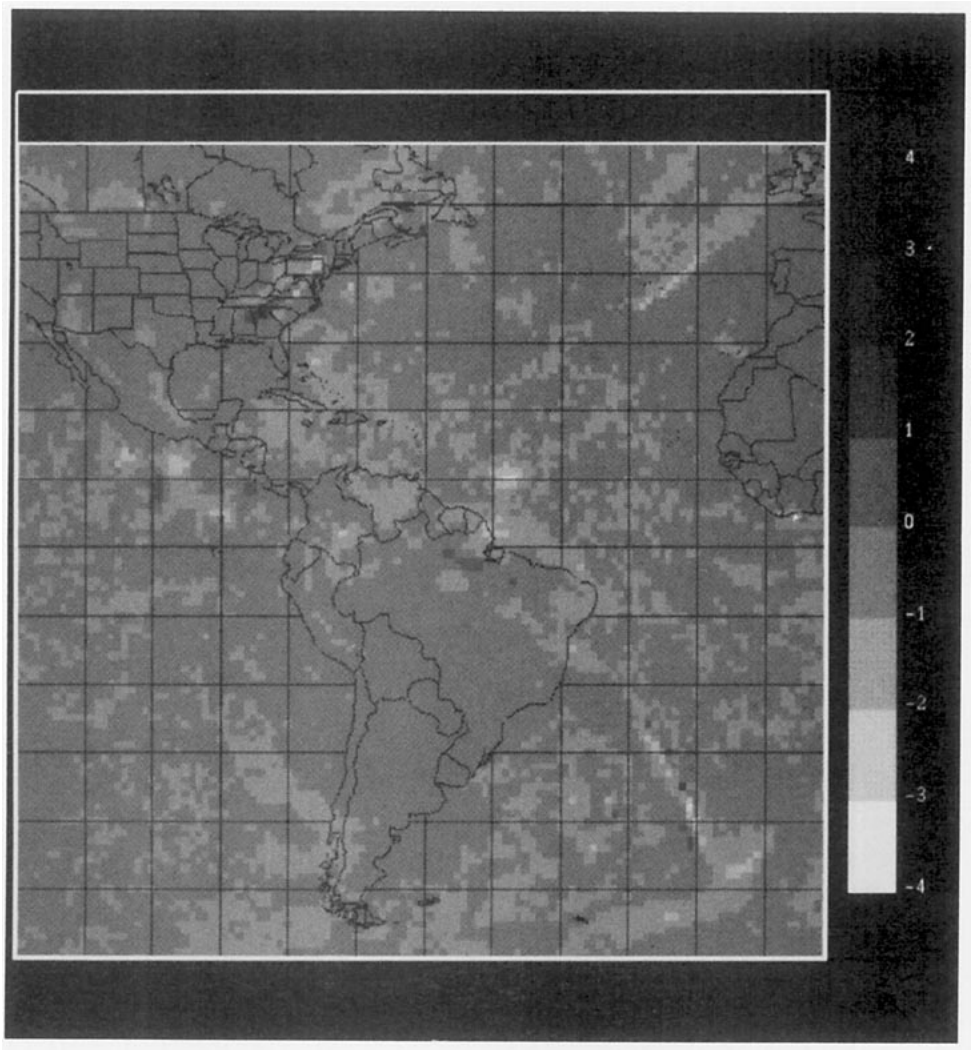

FIG. 3. Difference (mm h^{-1}) of 6-h minus 18-h forecasts valid at 0000 UTC 27 June 1994.

The 2D correlation is obtained from all possible distance pairs (∂x, ∂y, in gridpoint units) between grid points. A plot of $C(\partial x, \partial y)$ reveals the level of isotropy of the autocorrelation function. The physical distance between 1° grid points in the north–south direction is fixed at $d_0 = 111$ km, but it varies with latitude (L) in the east–west direction. More specifically, the physical distance between sites separated by (∂x, ∂y) gridpoint units is

$$d = d_0(\partial x^2 \cos^2 L + \partial y^2)^{1/2}. \quad (5)$$

In the binning process, the average value of $\cos^2 L$ is used, which between latitudes L_1 and L_2 in radians is

$$\overline{\cos^2 L} = 0.5 + 0.25[\sin(2L_2) - \sin(2L_1)] \times (L_2 - L_1)^{-1}. \quad (6)$$

Three 120° × 120° subdomains were examined, each between 60°S and 60°N, and starting at longitudes 0°, 120°E, and 240°E. Figure 2 shows the 6-h forecast rain rate for the subdomain starting at 240° and Fig. 3 shows the difference between the 6- and 18-h rain rate forecasts valid at 0000 UTC 27 June 1994. It is noted that phase differences are largest in precipitating areas associated with frontal zones, as recognized by the shape of the precipitation pattern in Fig. 2. The main features in the difference map of Fig. 3 resemble those present in the 6- or 18-h forecasts. The field of autocorrelation is nearly isotropic (Fig. 4), and an excellent fit can be obtained (Fig. 5) from (3), yielding $L_b = 76.3$ km, a value close to the average of 70 km found in the previous section. This subdomain coincides with that used for the sensitivity experiments described in section 3; therefore, the correlation length scale ($\sim$70 km) and the isotropy assumption seem appropriate for these experiments. The subdomain starting at 0° yielded $L_b = 107.9$ km and that starting at 120°E yielded $L_b = 92.0$ km; both with a high degree

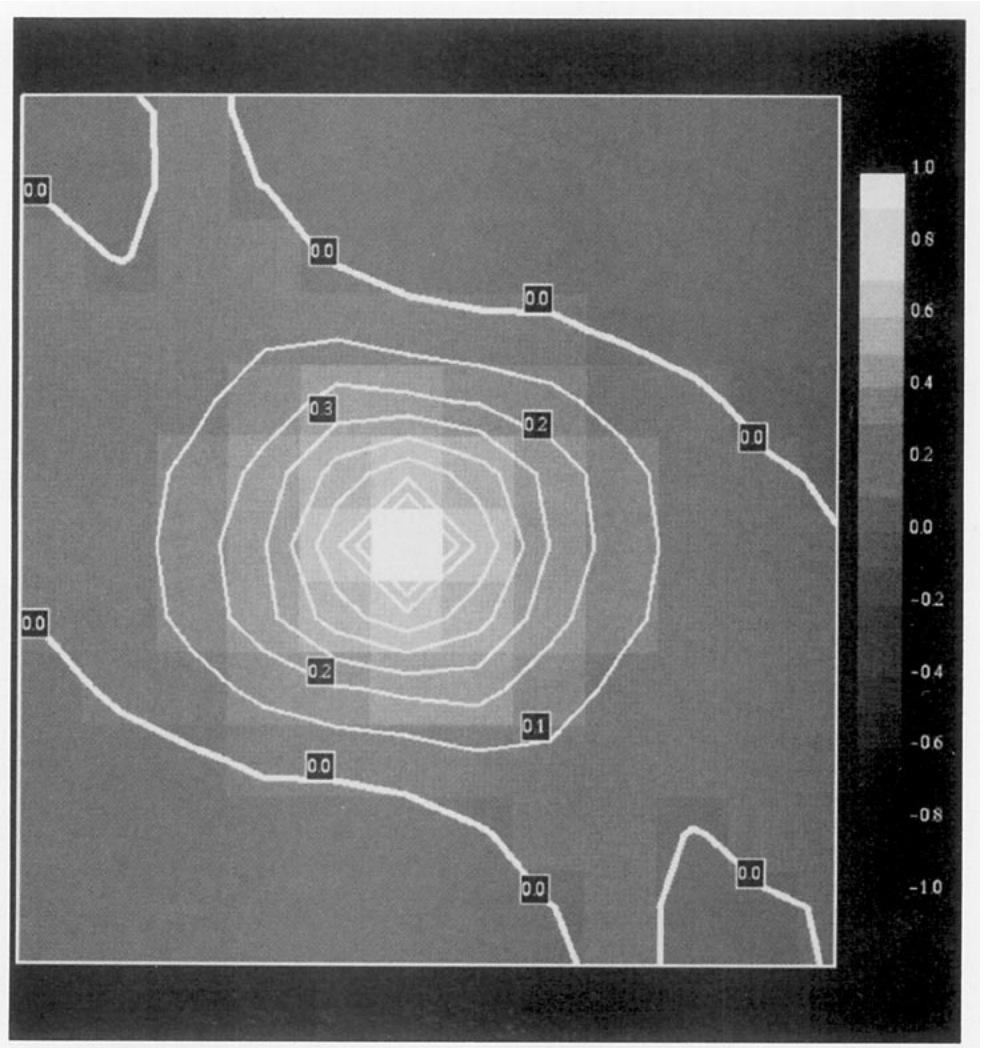

FIG. 4. Autocorrelation function extracted from Fig. 3. Pixels represent unit grid size distances (∂x, ∂y). Only the center portion of the pattern is shown: center pixel (white) represents zero distance.

of isotropy. In the latter subdomains (not shown), it was verified that the precipitation was organized at a slightly larger scale, especially over tropical oceans, as opposed to the finer structure shown in Fig. 2. A 40° × 40° area centered on Japan had a mean L_b of 66 km, again similar to that obtained over the same area in the previous section, but the 2D pattern of correlation was slightly elongated in the northeast–southwest direction. Subdomains were examined in regions of fronts oriented at some angle with respect to the east–west direction. There the horizontal correlation structure was strongly anisotropic (elongated) at the same angle as the front. Bellon et al. (1993) have shown the importance of using anisotropic interpolation in regions where rain patterns are elongated. Our results suggest that further research is warranted along the lines of detecting anisotropic error structures in real time by the method of forecast differences. Such studies are beyond the scope of the present paper. The important point that we wish to convey is that there is hope of defining realistic model error structures locally and to relax the assumption of isotropy.

3. Example of analysis

To assess the sensitivity of the analysis to variations in the satellite-to-model error ratios, five analyses at 1200 UTC 27 June 1994 were made, each with a different error ratio. For all experiments, the values of L_0 and L_b are fixed at 70 km. The analysis grid is Gaussian at 1° × 1°, while the satellite observations are on a latitude–longitude grid also at 1° × 1°. The two grids share the same longitude boundaries, but the latitudes have an offset of 0.5°. For each grid point, observations up to 300 km are considered, implying typically 25 observations, hence a 25 × 25 matrix system to solve for the weights in (2). That system is solved by an iterative procedure using a steepest-descent algorithm

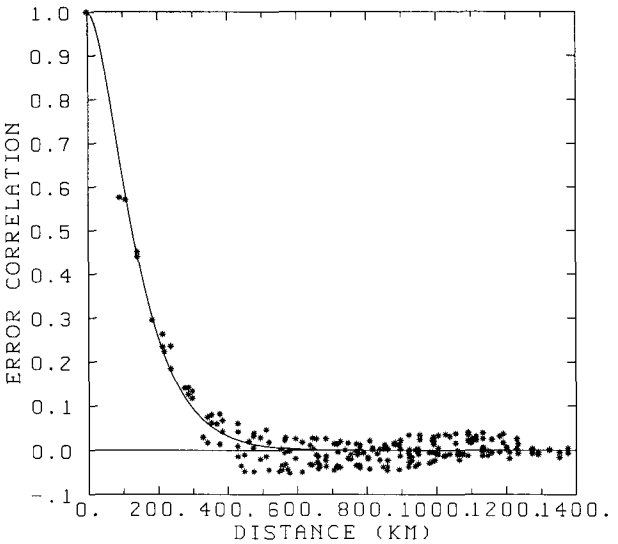

FIG. 5. Fit of the autocorrelation data in Fig. 4 as a function of distance; a length scale L_b = 76.3 km is found.

(Faddeev and Faddeeva 1963). The assumption of a locally uniform background error was used. It was found that unrealistic weights can occur in regions containing sharp discontinuities of σ_b because the background error correlation, derived from overall statistics, is not representative of such situations. These problems are avoided if the assumption of a locally uniform background error is used. Specifically we solve the system:

$$\sum_{j=1,N}\left[\mu_{ij}+\nu_{ij}\left(\frac{\sigma_0}{\sigma_b}\right)_i\left(\frac{\sigma_0}{\sigma_b}\right)_j\right]W_j=\mu_{ai};\quad i=1,N. \quad (7)$$

The analyses are obtained from a 6-h forecast issued at 0600 UTC of the selected day and satellite estimates based on 1200 UTC images using the GG94 algorithm, that is, based on the rain rate means RR_s listed in Table 1. Figure 6a shows the satellite estimates for a portion of the *GOES-7* satellite disk. There are a few missing lines near 30° latitude. The rainfall analysis is equal to the 6-h forecast where there is no data within 300 km. Most estimates in Fig. 6a are based on the IR scheme since cloud albedo information was available only on the extreme eastern portion of the GOES disk. Figure 6b shows the corresponding 6-h forecast. A good degree of similitude between the two pieces of information is apparent, which is in accordance with earlier statements on the relatively low occurrence of rain versus no rain conflicts between the model and satellite estimates. At the CMC, humidity profiles derived from a VIS–IR classification (Garand 1993) are used in the operational humidity analysis and therefore contribute to the similarity between model and satellite rain rate patterns. However, in this particular case, such humidity profiles were not used at 0600 UTC that day.

The five analyses were made over the 70° × 70° domain, all using the four error categories defined in section 2. In each experiment the satellite rain rate estimates were identical, namely, the values based on Table 1, but with different values of the satellite-to-background error ratios. These ratios σ_s/σ_b are listed in Table 4 for the five experiments. In "EQUAL" the standard deviation ratios are all set to unity, whereas in "PERFO" they are set to 0.1, simulating a nearly perfect satellite observation. In "IR" and "VIS–IR" the ratios are based on a compromise between the June and July/August results shown in Table 2. The "SSM/I" test uses VIS–IR ratios arbitrarily multiplied by 70% in order to simulate higher quality retrievals that could be available from microwave imagery (the Special Sensor Microwave/Imager: SSM/I). An experiment using weights based on the 22 classes was also made, but the results turned out to be very similar to those made using the corresponding (IR or VIS–IR) four categories. For the IR, VIS–IR, and SSM/I experiments, a fifth category (listed in Table 4) is added: when class 22 occurs (rain rate of 4 mm h^{-1}), the ratio is set at 0.5 (0.35 for SSM/I) if the model infers no or little rainfall (<0.3 mm h^{-1}); the rationale for this was previously discussed in section 2.

The resulting analyses for PERFO, EQUAL, and VIS–IR are shown in Figs. 6c–e. In the PERFO experiment, the analysis closely resembles the satellite estimates, but some smoothing extending to the immediate neighbors is apparent due to the length scale of 70 km; such a length scale implies an influence of the observation up to about 250 km (Fig. 1). Comparison of the EQUAL and VIS–IR analyses reveals a good degree of similitude in terms of location and intensity of rainfall. Nevertheless, the positive effect of the categorization is particularly clear in regions where the model infers rain and the satellite disagrees. These regions include the northeast of Cuba and south of Guatemala near 10°N, 90°W, where the VIS–IR analysis reduces the precipitation inferred by the model significantly, while EQUAL, as expected, blends the two estimates equally. The VIS–IR scheme also maintains sharper contrasts, especially where maximum estimates of 4 mm h^{-1} occur. Figure 6f shows the difference between the analysis and the background ($A - B$) for the VIS–IR experiment. Strong positive regions are mostly associated with the 4 mm h^{-1} estimates (class 22), which have a strong weight. Largest negative sectors (white) are associated with category 2 (satellite infers no rain, models disagrees).

In the domain of Fig. 6, there were 1480 grid points where either the model or the nearest satellite observation (distant by about 65 km) or both had estimates superior to 0.1 mm h^{-1}. For those grid points, the rms difference between the analysis and the model background $|A - B|$ and between the analysis and nearest observation $|A - O|$ are listed in Table 4 along with the corresponding mean difference. For the ensemble

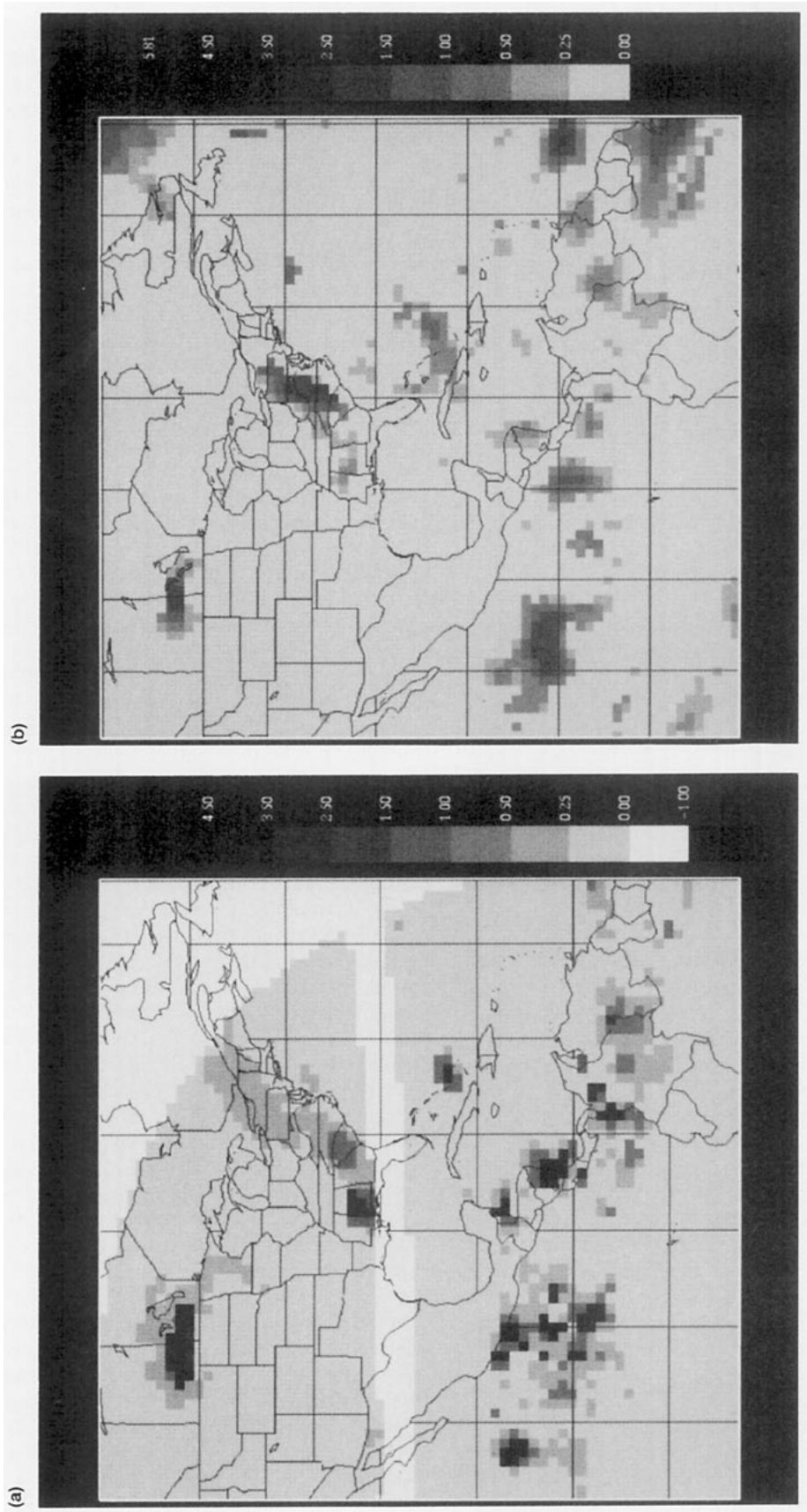

FIG. 6. (a) Satellite estimate of rain rate at 1200 UTC 27 June 1994; (b) 6-h forecast of rain rate valid at the same time. Resulting analysis of rain rate corresponding to (c) PERFO, (d) EQUAL, and (e) VIS–IR weights; VIS–IR analysis increments in (f). Units are millimeters per hour. Weights listed in Table 4.

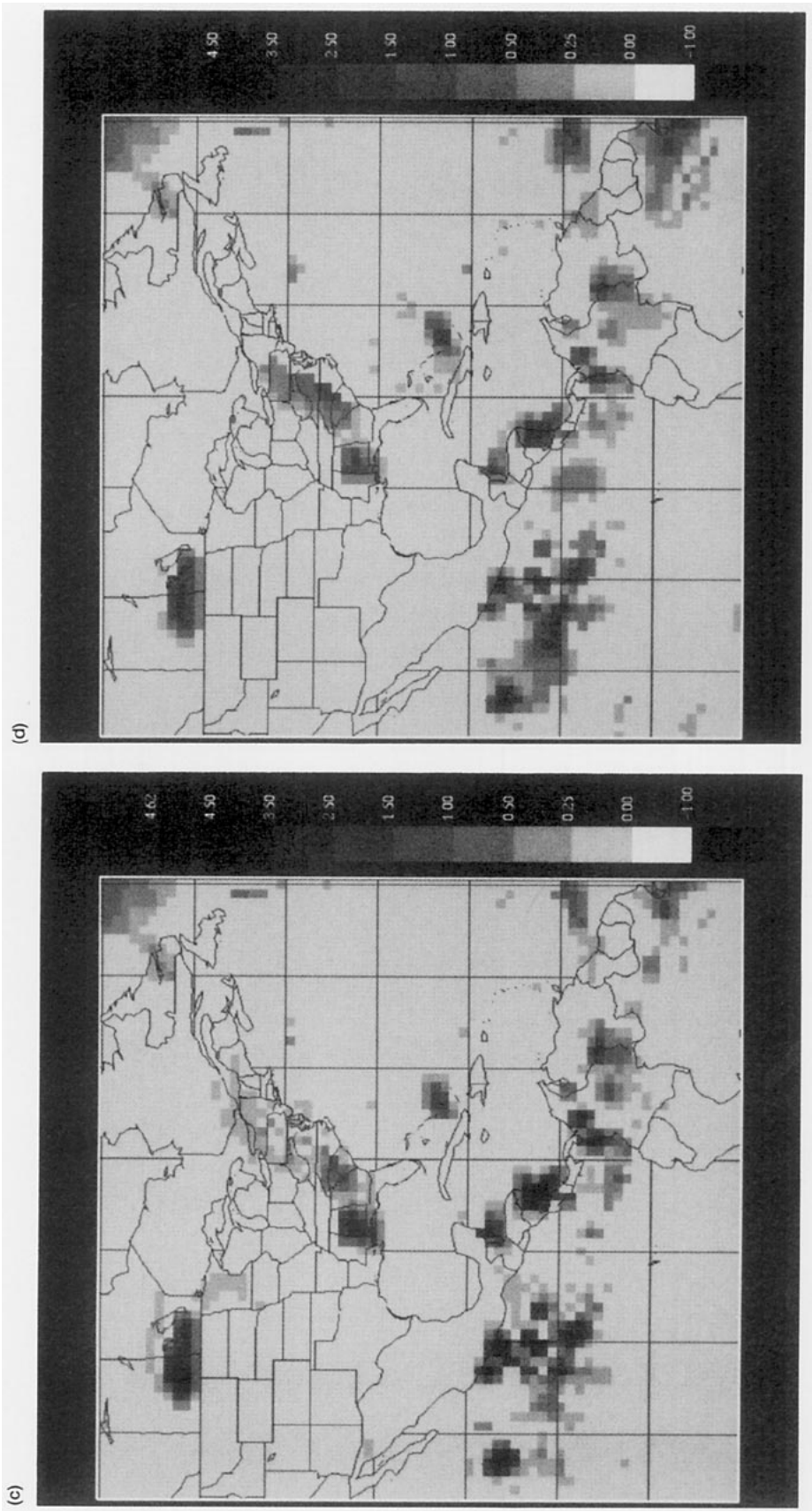

FIG. 6. (*Continued*)

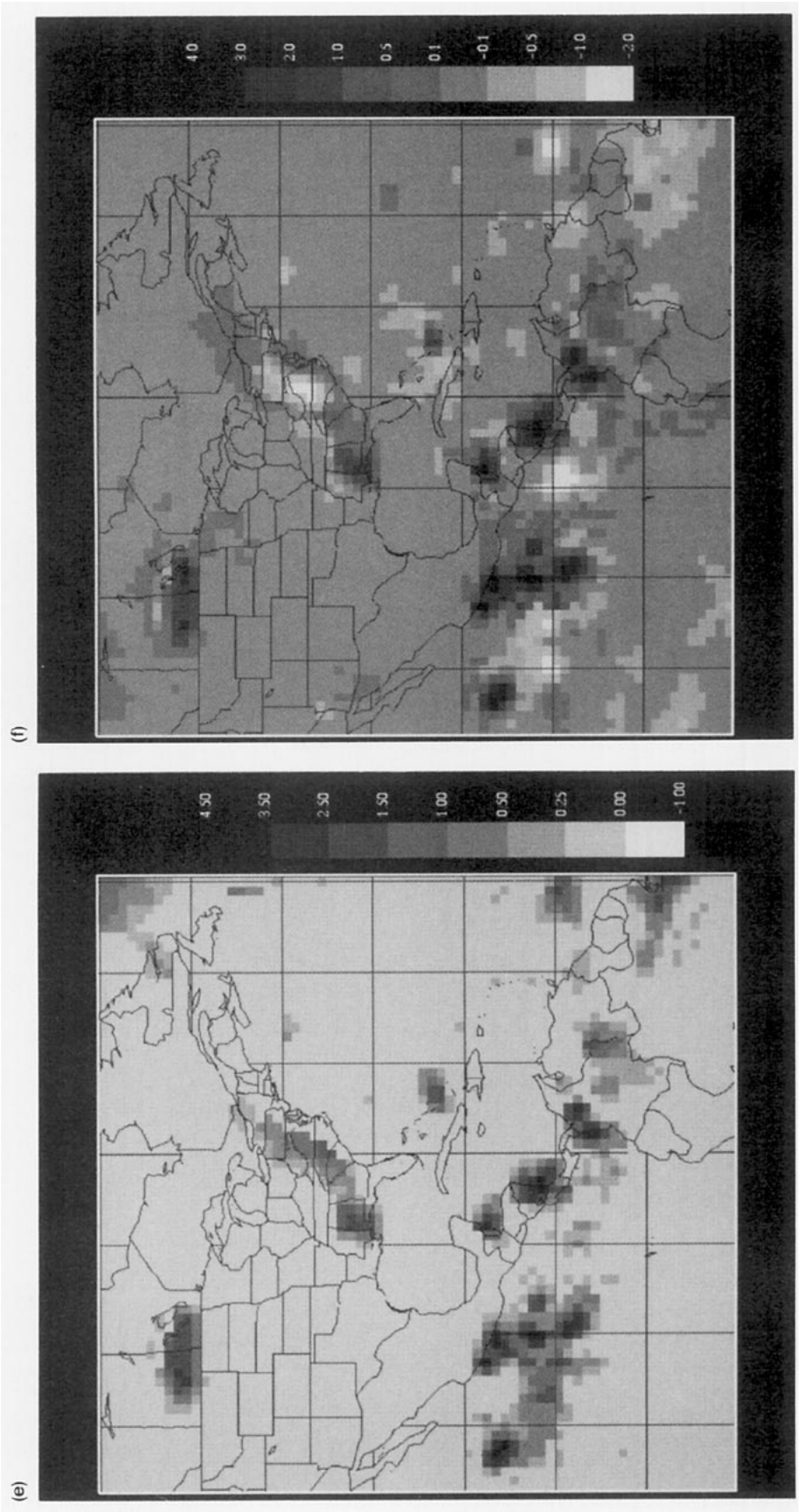

FIG. 6. (*Continued*)

TABLE 4. Satellite-to-model rms ratios by joint satellite–model rainfall category for five observing simulations: equal (EQUAL) weights, IR and VIS–IR schemes, SSM/I assumed errors, and nearly perfect observations (PERFO). Bias and rms distance of the resulting analysis to guess field ($A - B$) and to the nearest observation ($A - O$) are listed for the case shown in Fig. 6 along with the mean analyzed rain rate. These statistics are based on 1480 points where either the model or the observation infers rainfall.

	Standard deviation ratio σ_s/σ_b				
Category	EQUAL	IR	VIS–IR	SSM/I	PERFO
1	1.00	0.90	0.85	0.60	0.10
2	1.00	1.00	0.92	0.64	0.10
3	1.00	0.68	0.40	0.28	0.10
4	1.00	1.00	0.63	0.44	0.10
5	1.00	0.50	0.50	0.35	0.10
	Field statistics (mm h^{-1})				
$\overline{A-B}$	0.09	0.22	0.17	0.18	0.18
$\overline{\lvert A-B\rvert}$	0.45	0.78	0.74	0.81	0.89
$\overline{A-O}$	−0.11	0.02	−0.03	−0.02	−0.02
$\overline{\lvert A-O\rvert}$	0.58	0.48	0.45	0.41	0.39
$\bar{A}$	0.38	0.51	0.46	0.47	0.47

of 1480 points, the mean observed rain rate was 0.49 mm h^{-1}, and the mean background rain rate was 0.29 mm h^{-1}: there was an overall ($O - B$) difference of 0.20 mm h^{-1}. The mean analyzed rain rate, A, shows that all analyses, with the exception of EQUAL, tend to produce an overall mean rain rate similar to that of the observations. As expected, the analysis gets closer to the observations and farther away from the background as σ_s/σ_b decreases. For example, the distance $|A - B|$ in EQUAL is about one-half that in PERFO. However, that distance is slightly smaller in VIS–IR than it is in the IR experiment (by 0.04 mm h^{-1}) despite a significantly lower ratio σ_s/σ_b. This is caused by the effect of the horizontal correlations and the ensemble of participating observations, which make possible an analysis at a grid point lying outside the range defined by the background and the nearest observation; in such situations the analysis will be closer to both the nearest observation and the background as the weight of the observation increases.

Tests were conducted using observations up to 200 km, that is, the nearest nine observations (rather than about 25). The results were only marginally different, with distant 4 mm h^{-1} observations increasing some increments by about 0.4 mm h^{-1}; this was expected given the sharp decrease of error correlation with distance. Tests were also made assuming no correlation of errors for observations assumed to belong to a different category (differing by more than 0.25 mm h^{-1}); resulting analysis increments usually differed by less than 10%, but with local differences up to 0.8 mm h^{-1} noted in the vicinity of maximum rain rates; the net effect there was to reduce the maxima as rain rates of differing types were considered more like independent information. Perhaps this latter approach would be the best to take. Finally, tests were made assuming no correlation at all for observation errors ($v_{ij} = 1$ for $i = j$; 0 otherwise). The difference between VIS–IR analyses without and with error correlation is shown in Fig. 7. The satellite data had clearly more weight, with higher analyzed rain rates (up to 0.9 mm h^{-1} in southern Manitoba) in sectors where the observed rain rates were higher than the background and lower analyzed rain rates in the reverse situation (typically 0.2–0.5 mm h^{-1} over the eastern United States and over the ocean to the southwest of Mexico).

4. Discussion

This study has shown that forecast models provide rainfall-rate fields of sufficient accuracy to be used with observations in an objective analysis scheme. Over the oceans, a possible scenario would involve an analysis combining 6-h forecast rain-rate fields, VIS, and IR estimates from geostationary satellites and microwave estimates from polar orbiters, using channels such as those of SSM/I. Over land, observations from ground stations would contribute, but the CMC has found these rain gauge measurements to have a significant representativeness error relative to model fields. As models produce forecasts at higher resolution (responding to topographical effects), we expect this problem to diminish. Radar observations, properly calibrated, also represent a very valuable data source. In any case, there is a need to average or sample the data to approximately the same scale and to quantify the observation errors at that scale.

A key element of this study was the estimation of the observation and background errors. We found it very desirable to categorize the errors in at least a few classes; this is not customary for conventional observations in operational weather analysis but has been used with some forms of satellite data (Sullivan et al. 1993). The concept of joint model–observation categories of errors was proposed, with emphasis on the satellite-to-model ratios rather than the determination of each individual component. We found this ratio to be very low in the case when the satellite does not infer rainfall while the model does. In the converse situation, the satellite and model errors appear to be roughly equivalent for the VIS–IR technique used, but we expect microwave satellite and radar estimates to show some advantage in that case.

Another important aspect was the specification of the horizontal correlation of model and satellite errors. Using a conventional collocation method, these were found to be negligible beyond 250 km. We also investigated an alternative approach for computing the model error correlation function by using the difference between 6- and 18-h forecasts valid at the same time. This approach yields a very similar correlation function for large domains, but not locally, and suggests a means

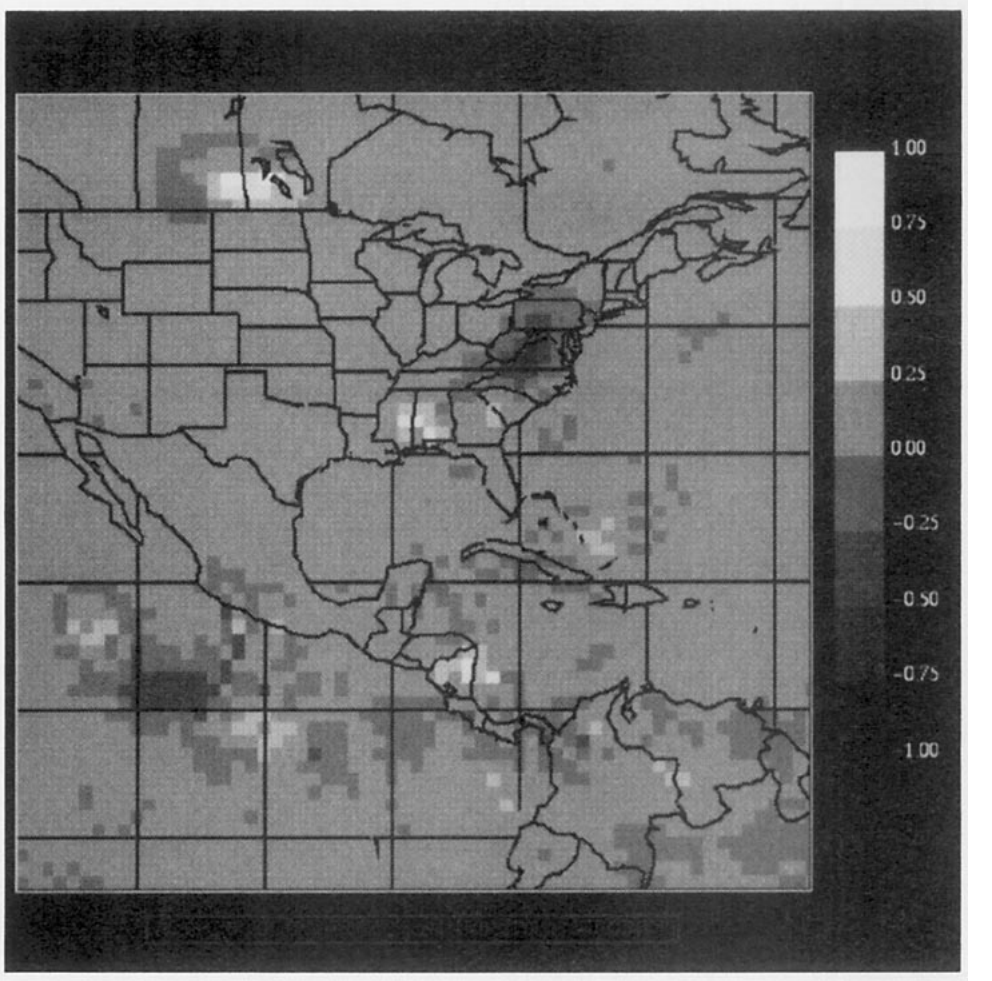

FIG. 7. Difference between the VIS–IR rainfall analysis (mm h^{-1}) performed *without* consideration of the horizontal correlation of observation errors minus that performed *with* (i.e., Fig. 6e) consideration of this correlation.

to obtain maps of the error standard deviation and to relax the current hypothesis of error isotropy.

The applications of a near-real time (delay of a few hours) analysis of rainfall are numerous. Global climatologies of rainfall are only starting to be assembled from different sources. The objective analysis approach offers a good framework to accomplish this task without having to assemble massive amounts of data after the fact. There is a need for a timely rainfall analysis that can serve as input to soil moisture schemes within mesoscale prediction models (Smith et al. 1994). Finally, rainfall analyses can be used to improve the initial state of the atmosphere via diabatic or physical initialization (see, e.g., Puri and Miller 1990; Krishnamurti et al. 1994) or through some humidity enhancement in precipitating areas. Although the issues of error estimation and validation of satellite techniques remain challenging, a global analysis of instantaneous rainfall appears feasible from the current availability of satellite estimates and from the quality of short-term forecasts at a horizontal scale on the order of 100 km.

REFERENCES

Adler, R. F., A. J. Negri, P. R. Keehn, and I. M. Hakkarinen, 1993: Estimation of monthly rainfall over Japan and surrounding waters from a combination of low-orbit microwave and geosynchronous IR data. *J. Appl. Meteor.*, **32,** 335–356.

Arkin, P. A., and P. Xie, 1994: The global precipitation climatology project: First algorithm intercomparison project. *Bull. Amer. Meteor. Soc.*, **75,** 401–419.

Bellon, A., M. Duncan, and G. L. Austin, 1993: A non-isotropic gauge interpolation scheme applied to the Montreal rainstorm of 14 July 1987. *Atmos.–Ocean,* **31,** 27–56.

Bhargava, M., and M. Danard, 1994: Application of optimum interpolation to the analysis of precipitation in complex terrain. *J. Appl. Meteor.*, **33,** 508–518.

Cheng, M., R. Brown, and C. G. Collier, 1993: Delineation of precipitation areas using Meteosat infrared and visible data in the region of the United Kingdom. *J. Appl. Meteor.*, **32,** 884–898.

Courtier, P., J. C. Derber, R. M. Errico, J. F. Louis, and T. Vukicewic, 1993: Important literature on the use of adjoint, variational

methods and the Kalman filter in meteorology. *Tellus,* **45A,** 342–357.

Daley, R., 1991: *Atmospheric Data Analysis.* Cambridge University Press, 457 pp.

Faddeev, D. K., and V. N. Faddeeva, 1963: *Computational Methods of Linear Algebra.* W. H. Freeman, 620 pp.

Garand, L., 1993: A pattern recognition technique for retrieving humidity profiles from Meteosat or GOES imagery. *J. Appl. Meteor.,* **32,** 1592–1607.

——, 1994: Assimilation of satellite humidity retrievals at the CMC. Preprints, *Seventh Conf. on Satellite Meteorology and Oceanography,* Monterey, CA, Amer. Meteor. Soc., 397–399.

Grassotti, C., and L. Garand, 1994: Classification-based rainfall estimation using satellite data and numerical forecast model fields. *J. Appl. Meteor.,* **33,** 159–178.

Krishnamurti, T. N., G. D. Rohaly, and H. S. Bedi, 1994: On the improvement of precipitation forecast skill from physical initialization. *Tellus,* **46A,** 598–614.

Lorenc, A. C., 1981: A global three-dimensional multivariate statistical interpolation scheme. *Mon. Wea. Rev.,* **109,** 701–721.

Mitchell, H. L., C. Charette, C. Chouinard, and B. Brasnett, 1990: Revised interpolation statistics for the Canadian data assimilation procedure: Their derivation and application. *Mon. Wea. Rev.,* **118,** 1591–1614.

Negri, A. J., and R. F. Adler, 1993: An intercomparison of three satellite infrared rainfall techniques over Japan and surrounding waters. *J. Appl. Meteor.,* **33,** 357–373.

Parrish, D. F., and J. C. Derber, 1992: The National Meteorological Center's spectral statistical-interpolation analysis system. *Mon. Wea. Rev.,* **120,** 1747–1763.

Puri, K., and M. J. Miller, 1990: The use of satellite data in the specification of convective heating for diabatic initialisation and moisture adjustment in numerical prediction models. *Mon. Wea. Rev.,* **118,** 67–93.

Rabier, F., and T. McNally, 1993: Evaluation of forecast error covariance matrix. ECMWF Tech. Memo. No. 195, 30 pp.

Rosenfeld, A., and A. C. Kak, 1982: *Digital Picture Processing.* 2d. ed. Vol. 1, Academic Press, 435 pp.

Rutherford, I. D., 1972: Data assimilation by statistical interpolation of forecast error fields. *J. Atmos. Sci.,* **29,** 809–815.

Shaw, D. B., P. Lönnberg, A. Hollingsworth, and P. Unden, 1987: Data assimilation: The 1984/185 revisions of the ECMWF mass and wind analysis. *Quart. J. Roy. Meteor. Soc.,* **113,** 533–566.

Smith, C. B., M. N. Lakhtakia, W. J. Capehart, and T. N. Carlson, 1994: Initialization of soil-water content in regional-scale atmospheric prediction models. *Bull. Amer. Meteor. Soc.,* **75,** 585–593.

Sullivan, J., L. Gandin, A. Gruber, and W. Baker, 1993: Observation error statistics for *NOAA-10* temperature and height retrievals. *Mon. Wea. Rev.,* **121,** 2578–2587.

Tanguay, M., and A. Robert, 1990: An efficient optimum interpolation analysis scheme. *Atmos.–Ocean,* **28,** 365–377.